LCLS-TN-05-21

A DESIGN REPORT FOR THE OPTICAL TRANSITION RADIATION IMAGER FOR THE LCLS UNDULATOR[1]

Bingxin Yang

Abstract

The Linac Coherent Light Source (LCLS), a free-electron x-ray laser, is under design and construction. Its high-intensity electron beam, 3400 A in peak current and 46 TW in peak power, is concentrated in a small area (37 micrometer in rms radius) inside its undulator. Ten optical transition radiation (OTR) imagers are planned between the undulator segments for characterizing the transverse profiles of the electron beam. In this note, we report on the optical and mechanical design of the OTR imager. Through a unique optical arrangement, using a near-normal-incidence screen and a multi-layer coated mirror, this imager will achieve a fine resolution (12 micrometer or better) over the entire field of view (8 mm × 5 mm), with a high efficiency for single-shot imaging. A digital camera will be used to read out the beam images in a programmable region (5 mm × 0.5 mm) at the full beam repetition rate (120 Hz), or over the entire field at a lower rate (10 Hz). Its built-in programmable amplifier will be used as an electronic intensity control.

Table of Contents

[1] Work supported in part by the DOE Contract DE-AC02-76SF00515.
This work was performed in support of the LCLS project at SLAC

1. Introduction

The Linac Coherent Light Source (LCLS), a free-electron x-ray laser is under design and construction. Ten optical transition radiation (OTR) imagers are planned between the undulator segments for the characterization of the electron beam's transverse profiles [1]. This document discusses the optical and mechanical design of the OTR imager to meet its physics requirements [2] and technical specifications [3]. This is an interim report for the design work performed to date by the ANL team for the LCLS project.

1.1 Design specifications

Table 1.1 lists the relevant parameters of the electron beam in the LCLS undulator [4]. These beam parameters evolve in time with the progress of the LCLS design. The Table 1.1 parameters are adopted from the parameter database maintained by Heinz-Dieter Nuhn on 5/25/2005. The performance specifications of the OTR electron beam imager are derived from the e-beam parameters (Table 1.2).

Table 1.1: Electron Beam Parameters in the LCLS Undulator [4]

Operation mode	Long wavelength	Short wavelength
X-ray photon energy (eV)	826.6	8266
Electron energy (GeV)	4.313	13.640
Single-bunch charge (nC)	0.2 – 1.0	0.2 – 1.0
Projected normalized emittance	3.0	2.0
Average beta function (m)	10.3	28.7
Projected rms beam radius (μm)	55	37
Bunch repetition rate (Hz)	120 (maximum)	
Vacuum chamber size (mm)	10 (H) × 5 (V)	
Quadrupole beam pipe ID (mm)	8	
Minimum aperture size (mm)	8 (H) × 5 (V)	

Table 1.2: Design Specification of the LCLS Undulator OTR Imager

Spatial resolution (rms)	12 μm
Minimum camera frame rate	10 Hz (full frame)
Maximum camera frame rate	120 Hz (region of interest)
Field of view	8 mm (H) × 5 mm (V)
Minimum imaging charge	0.2 nC @ 4.3 GeV
Maximum imaging charge	1.0 nC @ 13.6 GeV

The minimum operational charge (0.2 nC) appears to be most demanding for the imager design. Hence we decided to be less demanding on the spatial resolution (12 μm). Since the measured beam size is the quadrature sum of the true beam size and the system resolution, the specified 12-μm rms resolution will give us an error of 2 μm out of 37 μm (Fig. 1.1). This error is less than shot-to-shot fluctuation of the bunch size.

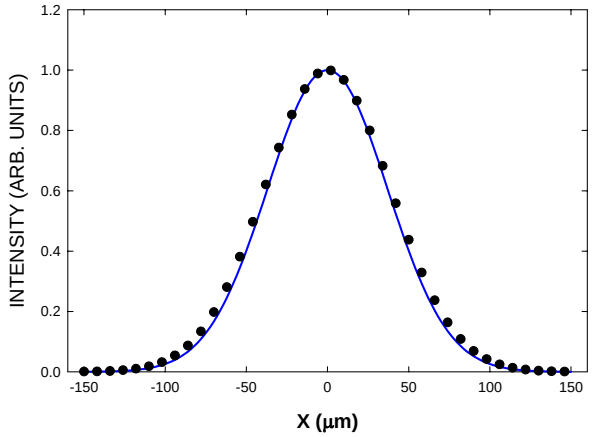

Figure 1.1: Illustration of effect of designed resolution: The solid line is a Gaussian beam profile with 37-μm rms width. The filled circles (8 μm/pixel) are the intensity profile of the same beam measured with 12-μm rms resolution.

1.2 Traditional design

It is the first time for us using a megapixel digital camera in an OTR imager. Hence many design decisions will be different from the traditional designs based on RS-170 analog television cameras. Throughout our discussion, we will use the APS bunch compressor camera [5] as an example of traditional design. That camera has the following features:

- One mirror (solid Mo or Al-coated silicon) at 45 degrees used as an OTR screen to convert the footprint of the electron beam into an optical source.
- CCD cameras with RS-170 interface, with an effective data set size of 511 (H) × 481 (V) × 8 (bit). No electronic amplifier was built in and the intensity was controlled by varying exposure time.
- A beam splitter to allow simultaneous operation of a high-resolution camera (beam size measurements) and a low-resolution camera (full field of view, beam finder) using different optical magnifications.
- A remotely controlled focus adjustment.
- A camera module that could be calibrated offline. Only focus needed to be fine tuned after installation, without change in optical magnification.

Many of these features will be changed in the current design. They will be discussed in the following sections.

2. Mechanical Design of the OTR Imager

Figure 2.1 shows a design of the camera module in its test configuration. The camera module is set for a fixed magnification of 1:1 and is mounted on a 6" × 10.25" custom vacuum cube (test station). Some mechanical design features are listed bellow:

(1) Two OTR screens will be installed in the vacuum enclosure. One of them will be designated as an in-vacuum spare. A vacuum motion feedthrough will be used to insert the OTR screen into the beam.

(2) An integral calibration target (pinhole) will be mounted with the OTR screens. It will be back-illuminated when inserted.

(3) The first lens assembly will be mounted directly over the viewport. It is adjustable in X and Y directions (both transverse directions) manually to center the images on the camera sensor.

(4) The second lens assembly will be driven by a stepper or a servo motor. Its motion along the optical axis will allow remote focus adjustment.

(5) An intensity control is not important with the low-charge operation, especially for cameras with variable gain. We included an iris diaphragm for compatibility with YAG screens.

(6) Both lens assemblies use standard 2-inch lens tubes with ample room for additional filters, polarizers, or lenses to be mounted.

(7) The camera is mounted with 5-degree tilt to compensate for the 5-degree tilt of the screen. The camera mount allows for camera azimuth rotation adjustment to orient the OTR screen image squarely.

(8) The camera will be shielded by > 5 mm tungsten in any direction. It is out of the way of any primary beam paths and primary scattering paths.

(9) The mounting base allows ± 3 mm adjustable range in both transverse directions for alignment.

Table 2.1: Optical Distance Between Major Components*

Optical Component	In Test Station	In Diagnostics Chamber
OTR screen	0.000"	0.000"
Center to first mirror (M1) distance	5.941"	2.723"
M1 to vacuum face distance	4.020"	8.516"
Vacuum face to first lens (L1) distance	2.000"	1.000"
L1 to second lens (L2) distance	2.200"	2.200"
L2 to second lens (M2) distance	6.135"	6.135"
M2 to third lens (M3) distance	3.000"	3.000"
M3 to CCD distance	2.500"	2.500"
L1 focal length (f_1)	300 mm	300 mm
L2 focal length (f_2)	300 mm	300 mm
Magnification	1	1

* Two configurations are listed: one for the Test Station and the other for Diagnostics Chamber.

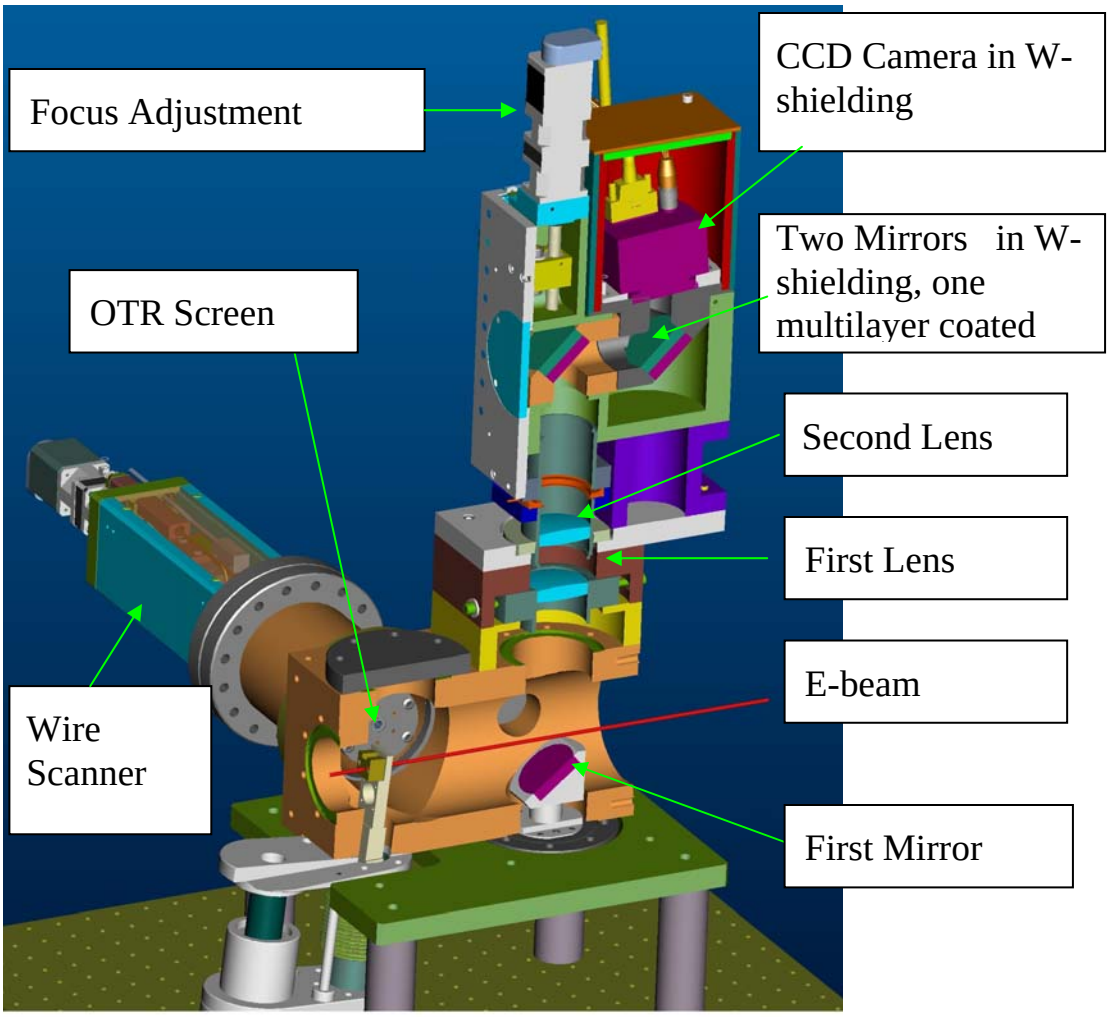

Figure 2.1: OTR camera module mounted on the test station.

3. Optical Design of the OTR Imager

Our challenge in optical design is to obtain high charge sensitivity while maintaining an adequate spatial resolution. In Section 3.1 we will discuss intensities of OTR light and efficiency of light collection. In Section 3.2 we will discuss some general considerations for the optical design, including an approach to achieve full-field focusing. In Section 3.3 we will discuss the need for limiting wavelength region for imaging, and the optimal approach for achieving it. In Section 3.4 we will discuss the criteria and selection of the digital camera. Finally, we will estimate the spatial resolution of the OTR imager in Section 3.5.

3.1 Absolute photon flux and efficiency

The spectral-angular distribution of transition radiation energy from an ultrarelativistic electron moving from vacuum into a metal surface can be written, in SI units, as [6]

$$\frac{d^2W}{d\omega d\Omega} = \frac{e^2}{4\pi^3\varepsilon_0 c}\frac{\beta^2\sin^2\theta}{\left(1-\beta^2\cos^2\theta\right)^2}, \tag{3.1}$$

where $\beta = v/c$ is the speed of the electron and θ is the angle between the detector and the specular direction (Figure 3.1). For relativistic electrons, the angular distribution is a highly symmetric hollow cone with an angular radius of $1/\gamma$.

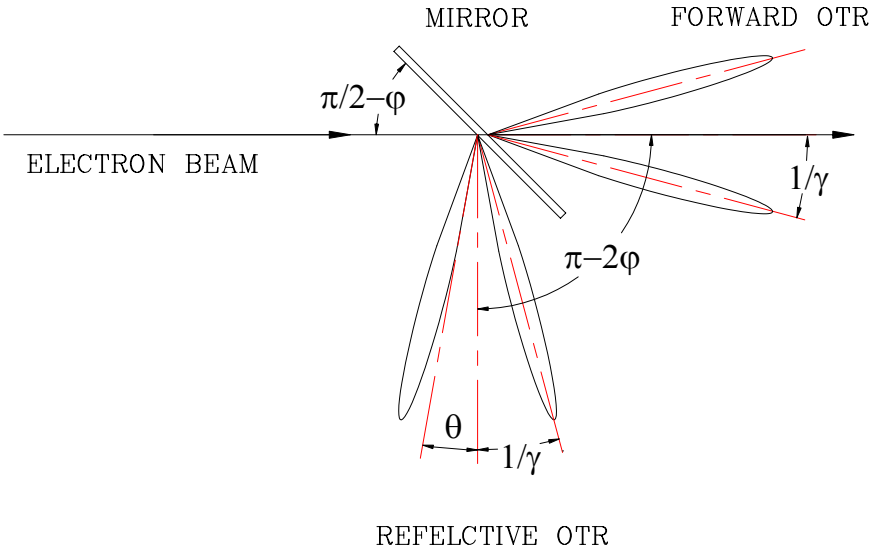

Figure 3.1: Optical transition radiation generated by passing an electron into a metal mirror.

[Absolute Photon Flux] Integrating over one side of the metal surface, we obtain the angle-integrated spectral intensity of OTR generated by one electron:

$$\frac{dW}{d\omega} = \frac{e^2}{4\pi^2\varepsilon_0 c}\left(\frac{1+\beta^2}{2\beta}\ln\frac{1+\beta}{1-\beta}-1\right) \approx \frac{e^2}{4\pi^2\varepsilon_0 c}\left(\ln 4\gamma^2 - 1\right). \tag{3.2}$$

Noting that the radiation energy W is related to photon number n by $dW/d\omega = \hbar\omega \cdot dn/d\omega$, we have

$$\frac{dn}{d\omega} = \frac{\alpha}{\pi\omega}\left(\ln 4\gamma^2 - 1\right) \approx \frac{\ln\gamma + 0.193}{215\omega}, \tag{3.3}$$

where $\alpha = e^2/4\pi\varepsilon_0\hbar c$ is the fine structure constant. If the optics select photons in a frequency range $\omega_1 < \omega < \omega_2$, the total number of photons the detector receives is

$$n(\omega_1,\omega_2) = \frac{\alpha\left(\ln 4\gamma^2 - 1\right)}{\pi}\ln\left|\frac{\omega_2}{\omega_1}\right| = \frac{\ln\gamma + 0.193}{215}\ln\left|\frac{\omega_2}{\omega_1}\right|. \tag{3.4}$$

Table 3.1 shows the total integrated photon flux for 0.2-nC charge for several selected electron energies. We have calculated the intensity for several selected wavelength regions:

- visible-light region [400 – 700 nm],
- warm-filtered region [500 – 700 nm],
- commercial achromat region / copper vapor laser mirror [470 – 645 nm],
- Nd:YLF laser mirror region [490 – 565 nm], and
- 70 nm bandpass filtered region [515 – 585 nm].

We can make the following observations from Table 3.1:

1. The photon flux generated by a 4.3-GeV electron is twice that generated by a 50-MeV electron.
2. The bandpass filter has a strong effect on the photon flux. A change of 75% in flux is expected when we reduce the entire visible-light spectrum with a 70-nm bandpass centered on 550 nm (the best region for many commercial achromat lenses).

Table 3.1: Total OTR Photon Flux per Electron Bunch for LCLS Operation Conditions

Electron energy	50 MeV	4.3 MeV	13.64 GeV
Bunch charge	0.2 nC	0.2 nC	1.0 nC
Passband = [400 nm, 700 nm]	**15.5×10^6**	30×10^6	169×10^6
Passband = [500 nm, 700 nm]	9.3×10^6	18×10^6	101×10^6
Passband = [470 nm, 645 nm]	8.8×10^6	17×10^6	95×10^6
Passband = [490 nm, 565 nm]	3.9×10^6	7.6×10^6	43×10^6
Passband = [515 nm, 585 nm]	3.6×10^6	**6.8×10^6**	39×10^6

[Geometric Efficiency] The fraction of photons entering a circular aperture with angular radius θ_0 can also be calculated from Eq. (3.1):

$$\eta_G \equiv \frac{\text{OTR photons collected}}{\text{OTR photons generated}} = \frac{\ln\left\{1+4\gamma^2\tan^2\frac{\theta_0}{2}\right\}+\frac{\cos\theta_0}{1+\gamma^2\sin^2\theta_0}-1}{\ln 4\gamma^2-1}. \tag{3.5}$$

Combining the two expressions above, we have an expression for the total number of photons generated by an electron bunch with charge Q, collected by an aperture of radius θ_0, and in the wavelength region [λ_1, λ_2]:

$$N_{collected}\left(Q,\theta_0,\lambda_1,\lambda_2\right) = \frac{\alpha}{\pi}\cdot\frac{Q}{e}\cdot\ln\left|\frac{\lambda_2}{\lambda_1}\right|\cdot\left[\ln\left(1+4\gamma^2\tan^2\frac{\theta_0}{2}\right)+\frac{\cos\theta_0}{1+\gamma^2\sin^2\theta_0}-1\right]. \tag{3.6}$$

In most practical situations, $\gamma\theta_0 >> 1$ and $\theta_0 < 1$, we have

$$N_{collected}\left[photons\right] \approx 3\times10^7\cdot Q\left[nC\right]\cdot\ln\left|\frac{\lambda_2}{\lambda_1}\right|\cdot\ln\left(\gamma\theta_0\right), \quad (\gamma\theta_0 > 3 \text{ and } \theta_0 < 1). \tag{3.7}$$

Figure 3.2 shows the calculated collection (geometric) efficiency as a function of optical aperture radius. It can be seen that as the electron energy increases, the OTR light collection efficiency is increasingly weighted in the forward direction. As a result, a cone with radius of 0.1 – 0.2 radian collects about 2/3 of the total OTR light generated when the electron energy is 4.3 GeV ($\gamma \sim 10^4$). It collects only ~ 45% when the electron energy is 50 MeV ($\gamma \sim 100$).

[Camera Pixel Size] Numerical simulation showed that the finite size of the camera sensor pixel makes the following contribution to the rms resolution [7]:

$$\sigma_{pixel} \approx \left(0.3+ f_{spill}\right)\Delta_x, \tag{3.8}$$

where f_{spill} is the fraction of charges spilled over to the nearest neighbor pixels. This indicates that a pixel size can be chosen anywhere below the design rms resolution. We choose, somewhat

arbitrarily,

$$\Delta_x \approx \frac{\sigma_x}{5} \to \frac{\sigma_x}{3} = 7.4 \to 12\,(\mu m)\,. \tag{3.9}$$

Pixel sizes of most commercial CCD cameras today fall in this range. Hence the optical magnification required for the undulator OTR imager is nearly 1:1. We showed a sample profile taken with 8 μm per pixel (0.22 σ_x) in Figure 1.1.

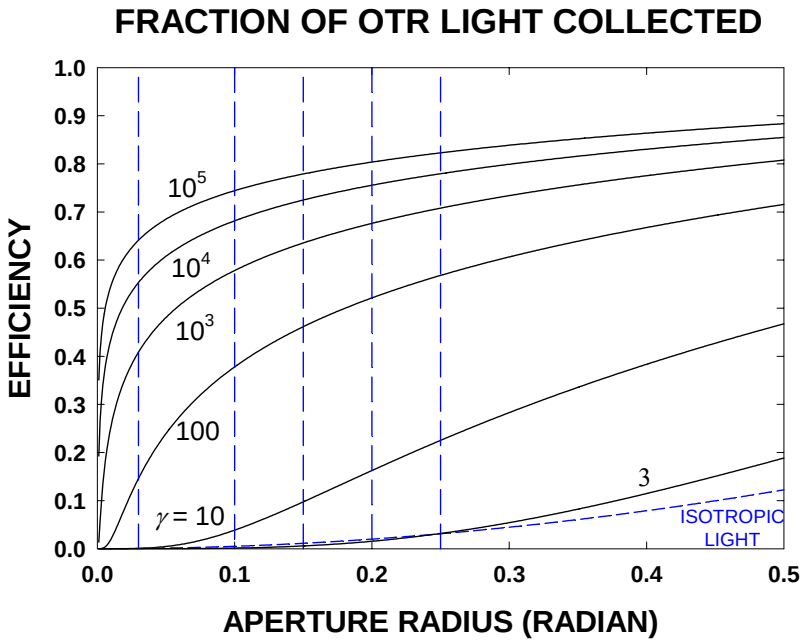

Figure 3.2: Geometric efficiency of the OTR imager as a function of angular radius of the aperture.

[Photoelectrons per CCD Pixel] The number of photons collected by the optics will spread over many camera pixels on the image plane. The maximum number of photons in a single pixel is given by

$$N_{pixel}\left[photons\right] = \frac{N_{collected}\left[photons\right]}{2\pi\sigma_x\sigma_y}\Delta_x\Delta_y\,, \tag{3.10}$$

where Δ_x and Δ_y are pixel sizes in the x and y directions, respectively. In most practical situations, the following estimate may be used:

$$N_{pixel}\left[photons\right] \approx 4.6\times10^6 \cdot Q\left[nC\right] \cdot \frac{\Delta_x\Delta_y}{\sigma_x\sigma_y} \ln\left|\frac{\lambda_2}{\lambda_1}\right| \cdot \ln\left(\gamma\theta_0\right). \quad (\gamma\theta_0 > 3 \text{ and } \theta_0 < 1). \tag{3.11}$$

To calculate the number of photoelectrons generated in each sensor pixel, we need to consider that (1) only a fraction (optical efficiency) of the photons are able to reach the camera sensor due to losses to unwanted reflection and absorption, (2) only a part of the area occupied by the sensor pixel is active, and (3) only a fraction of photons generate photoelectrons in the sensitive volume of the CCD (quantum efficiency). Note that some camera vendor lists the last two items separately, and others lump them together as effective quantum efficiency (Figure 3.3).

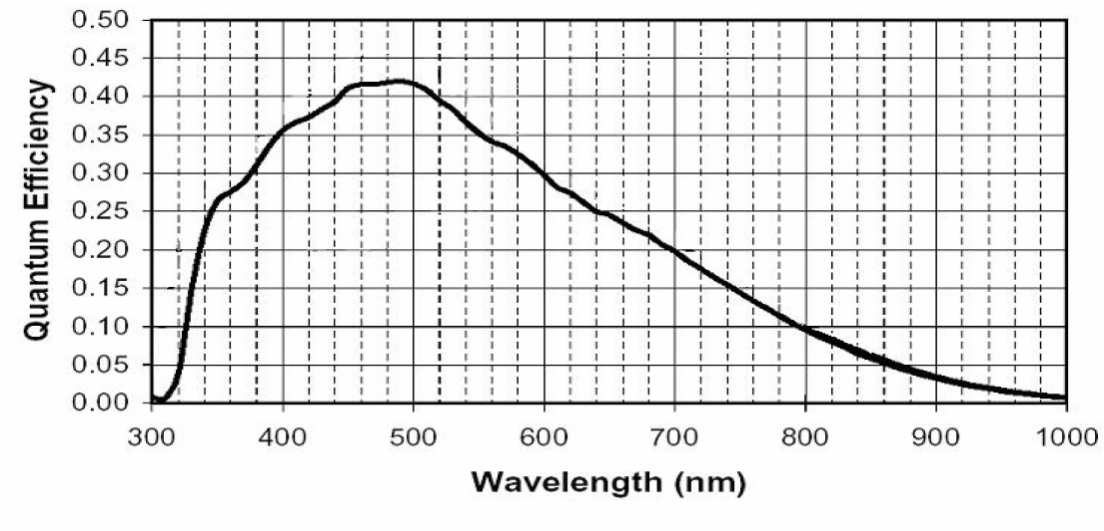

Figure 3.3: Imperx camera spectral response (www.imperx.com).

In Table 3.2 we estimate the number of photons and photoelectrons per CCD pixel, using typical LCLS beam parameters. The recommended operating configurations are highlighted in blue. Three factors contribute to the difference in photoelectrons per pixel at different electron energies: (1) high-energy electrons generate more light, (2) we used higher charge for high-energy electrons to mark the high end of the operation range, and (3) the electron beam is smaller at high electron energy. From Table 3.2, we can draw the following conclusions:

(1) We will use 490 nm – 565 nm band if the overall optical-quantum efficiency is 15% or higher (column highlighted in blue).

(2) We will use 475 nm – 645 nm band if the overall optical-quantum efficiency is 10% or lower (column not highlighted).

Table 3.2: Estimate of Maximum Number of Photoelectrons per CCD Pixel

Electron energy	50 MeV	**4.3 GeV**	4.3 GeV	**13.6 GeV**	13.6 GeV
Bunch charge	0.2 nC	**0.2 nC**	0.2 nC	**1.0 nC**	1.0 nC
Collection cone radius	0.1 rad	**0.1 rad**	0.1 rad	**0.1 rad**	0.1 rad
Beam size (σ_x, σ_y)	100 μm	**55 μm**	55 μm	**37 μm**	37 μm
Pixel size (Δ_x, Δ_y)	20 μm	**7.4 μm**	7.4 μm	**7.4 μm**	7.4 μm
Minimum photon wavelength	400 nm	**490 nm**	470 nm	**515 nm**	470 nm
Maximum photon wavelength	700 nm	**565 nm**	645 nm	**585 nm**	645 nm
Maximum # of photons per pixel	37 k	**15 k**	33 k	**194 K**	432 k
Total optical / quantum efficiency	10%	**15%**	10%	**15%**	10%
Max # of photo electrons per pixel	4 k	**2.2 k**	3.3 k	**29 K**	43 k

3.2 General considerations of optical design

[Camera Sensor Size] First we rewrite the design specification listed in Table 1.2 in terms of pixel units (Table 3.3). It can be seen that if we use camera sensors with over 1200 × 800 pixels, we will be able to image the entire field of view with the required resolution. We do not need to deal with the mechanical complication of variable optical gain (cross polarizers), nor the loss of optical efficiency from beam splitters.

Table 3.3: Resolution and Sensor Sizes in Pixel Units

Pixel size	7 μm	8 μm	9 μm	10 μm
Design resolution (12 μm rms)	1.7 pixel	1.5 pixel	1.3 pixel	1.2 pixel
Width of the field of view (H, 8 mm)	1143 pixel	1000 pixel	889 pixel	800 pixel
Height of the field of view (V, 5 mm)	714 pixel	625 pixel	556 pixel	500 pixel

[Maintaining Focus over the Field of View] To maintain focus over the entire field of view, we can consider the options shown in Figures 3.4 and 3.5. Figure 3.4A was used by Murokh et al. to image a low-energy electron beam using a normal-incidence OTR screen [8]. It uses an annular curved mirror to make an image free of chromatic aberrations. The method can be modified to use an annular flat mirror and lens optics (Figure 3.4B). It has lower cost and higher imaging flexibility, although its resolution will be dominated by chromatic aberration when white OTR light is used.

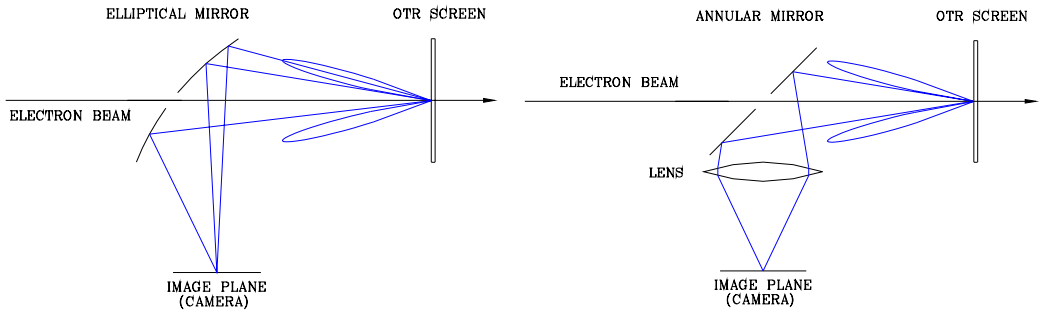

(A) (B)

Figure 3.4: Optics setup for using normal-incidence OTR screens.

For high electron energies ($\gamma > 100$), a good fraction of OTR light will be lost through the center hole (Figure 3.2). Hence we need to consider near-normal-incidence OTR screens. Figure 3.5A shows an OTR screen slightly tilted (~ 5°) from the normal incidence angle. An additional mirror was used to turn the optical axis 90° from the electron beam, making it easier to implement the imaging optics. The all-mirror achromatic imaging system (Figure 3.5B) will be our last resort for high-resolution, high-sensitivity applications.

To compensate for the small tilt angle ($\psi \sim 5°$) of the object plane, we also need to tilt the camera (ψ'). The two angles are related by $\tan\psi' = M \tan\psi$ [9], since the longitudinal magnification is M^2 for a lens system with a transverse magnification of M. Tilting of the image plate was a standard feature in many large cameras beginning in the late 19th century, and it has

been in use for beam diagnostics for at least five years [10]. However, many modern digital cameras use microlenses to improve light collection efficiency and do not permit large deviation from the normal incidence (Figure 3.6). The largest allowed angle is usually specified by the minimum *F*-number of the lens used for imaging. For example, if the camera accepts lenses with a minimum *F*-number of 1.4, the largest incidence ray angle at the camera sensor (ψ') is 0.5/1.4 = 0.36 radian = 20°.

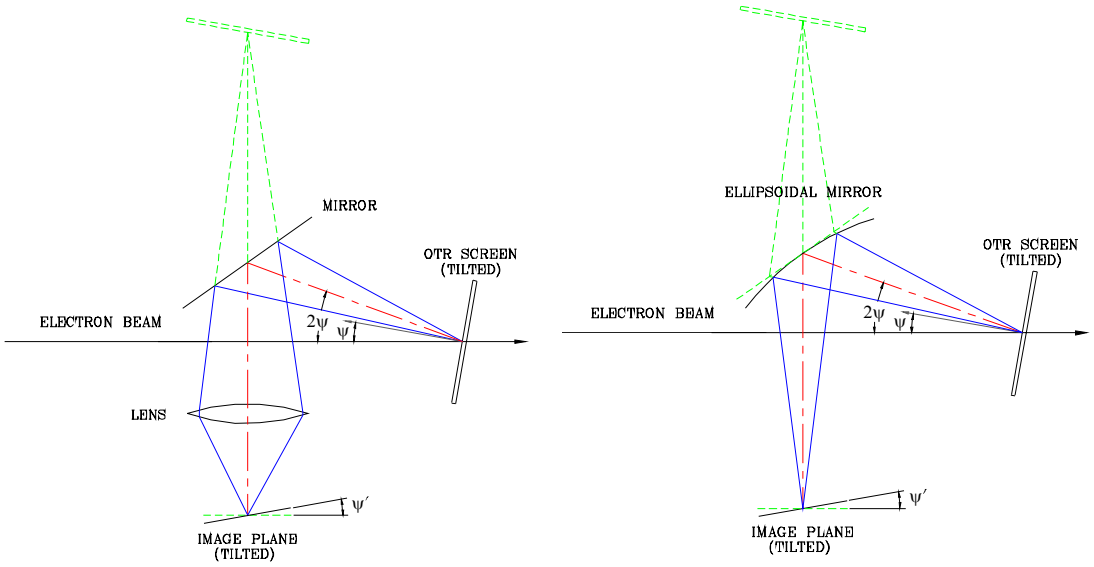

(A) (B)

Figure 3.5: Optics setup for using near-normal-incidence OTR screens.

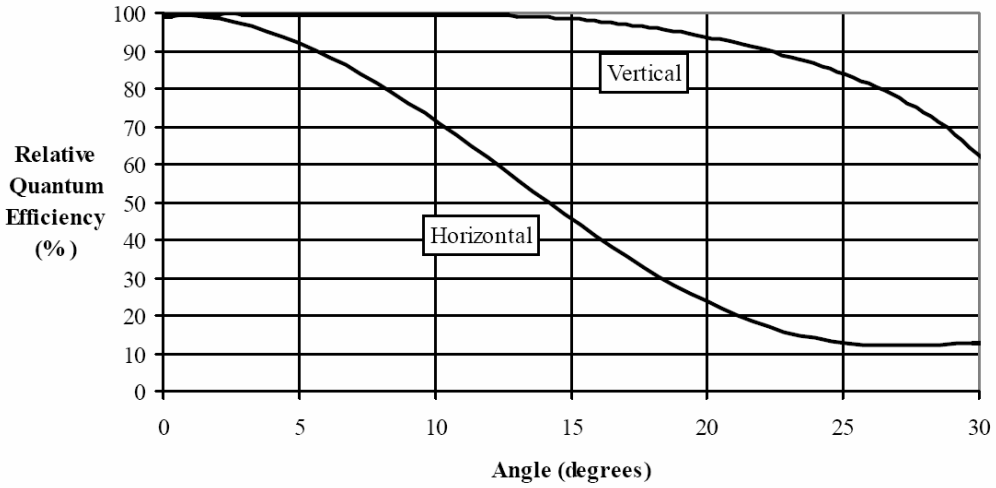

Figure 3.6: Kodak KAI-2020 (2M30) characteristic curve: quantum efficiency of the CCD as a function of the tilt angle of the incidence light (www.kodak.com).

For lower-energy applications, a reducing optics is needed ($M < 1$) to match the pixel size of the screen to that of the camera. Hence, a larger tilt of the OTR screen is allowed, giving more space for a larger field of view and the wakefield shielding tube.

3.3 Selecting wavelength

For a simple lens bound by two spherical surfaces, the curvatures of the surfaces can be chosen to make the lens to the desired focal lengths at one wavelength, as well as minimize the spherical aberration at that (or other) wavelength. Commercially available achromatic lens doublets are based on the simple design idea of using two media with different dispersion properties. The additional degree of freedom, the third surface radius, could be used to make the lens to have identical focal lengths at two different wavelengths. However, the common practice is to select three wavelengths – blue (λ_B), green (λ_G), and red (λ_R) – and to minimize the aberrations when rays of these three wavelengths are present (Table 3.4).

Table 3.4: Design Wavelengths for Achromatic Doublet Lenses

Manufacture	Blue (λ_B)	Green (λ_G)	Red (λ_R)
Melles Griot	480.0 nm	546.1 nm	643.8 nm
Newport	486.1 nm	546.1 nm	656.3 nm
Thorlabs	486.1 nm	587.6 nm	656.3 nm

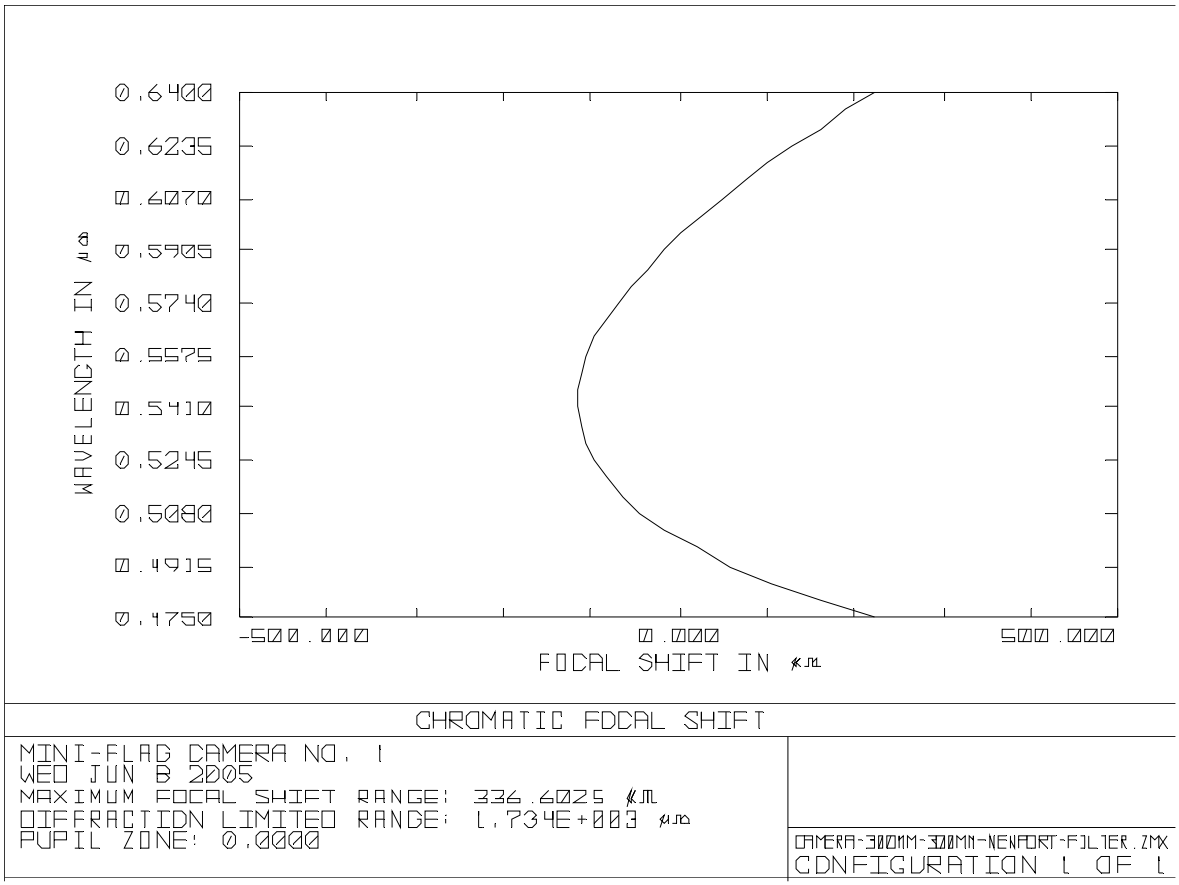

Figure 3.7: Focal length change of a pair of Newport 300 mm FL achromat doublet lenses (50.8-mm aperture diameter, a captured ZEMAX <analysis> screen).

Figure 3.7 shows the focal point shift of a pair of Newport achromat lens (300 mm + 300 mm FL, infinite conjugate, 1:1) as a function of wavelength. We can see that not only do we obtain

minimum spherical aberration at the design wavelength of 546.1 nm, we also get the best achromatic imaging at this wavelength, where the focal distance is nearly independent of the wavelength.

To reject photons outside of a narrow band of wavelengths, transmission interference filters are often used. Figure 3.8 defines terms commonly used in the specification of filters. Single bandpass filters with FWHM up to 70 nm are available commercially (Table 3.5). The peak transmission is normally in the range of 35% to 60%. Green process filter (color glass) with center wavelength 540 nm and bandwidth ~70 nm is also available.

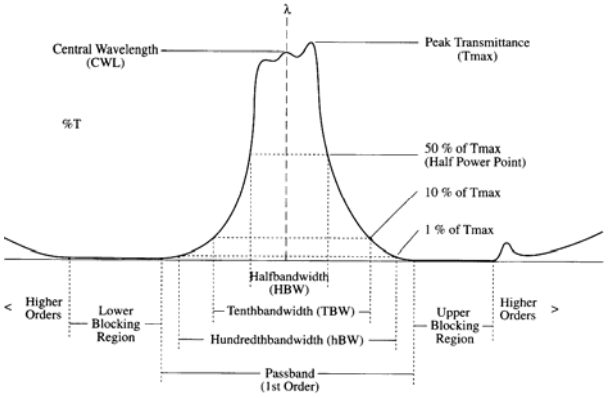

Table 3.5: Interference Bandpass Filters from CVI Laser Optics

CWL (nm)	HBW (nm)	Tmax (%)	Model #
550	3	40	F03-550.0-4-2.00
550	10	50	F10-550.0-4-2.00
550	25	50	F25-550.0-4-2.00
550	40	50	F40-550.0-4-2.00
550	70	60	F70-550.0-4-2.00

Figure 3.8: Specification of a bandpass filter.

To obtain a wider passband, one can use a long pass filter (LPF, 400 nm → 650 nm in 50 nm increments from CVI, Fig. 3.8) in combination with a short pass filter (SPF 450 nm → 700 nm in 50 nm increments from CVI, Fig. 3.9). The peak transmission of the combination is typically 50 – 65%.

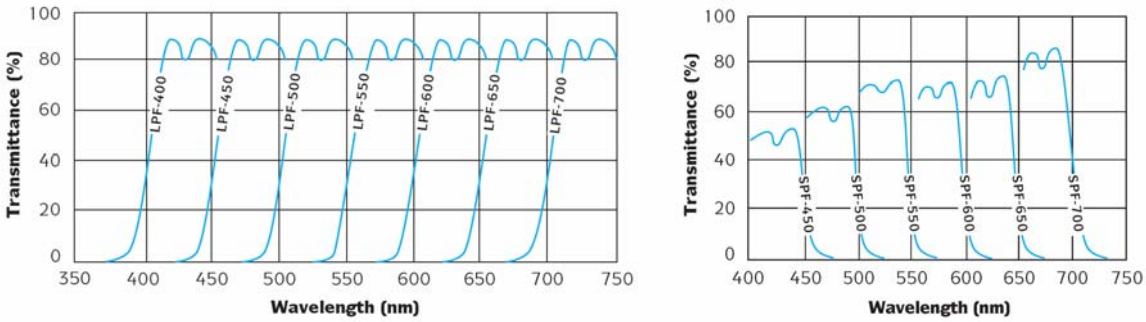

Figure 3.9: Edge filters from CVI Laser Optics.

Multilayer coated mirrors have higher efficiency than transmission bandpass filters at a slightly higher cost. Table 3.6 shows the approximate half-power passband of several laser mirrors available from CVI Laser Optics. To make use of the wavelength region of minimum wavelength variation, we need YL2 mirrors. To approximately cover the entire achromat lens design range, we need CV mirrors. Figure 3.10 shows the reflectivity of the two mirrors. Note that the reflectivity is different for P and S polarizations. An average of the two curves was used for unpolarized light in Table 3.6.

Table 3.6: Approximate Wavelength Region of Laser Mirrors from CVI Laser

Laser	**Nd:YLF**	HeCd	Argon-Ion	Argon-Ion	**Cu vapor**	HeNe
CVI part	**YL2**	HC1	AR2	AR1	**CV**	HN
Lower side HM	**490 nm**	400 nm	425 nm	425 nm	**470 nm**	540 nm
Upper side HM	**565 nm**	480 nm	580 nm	595 nm	**645 nm**	750 nm

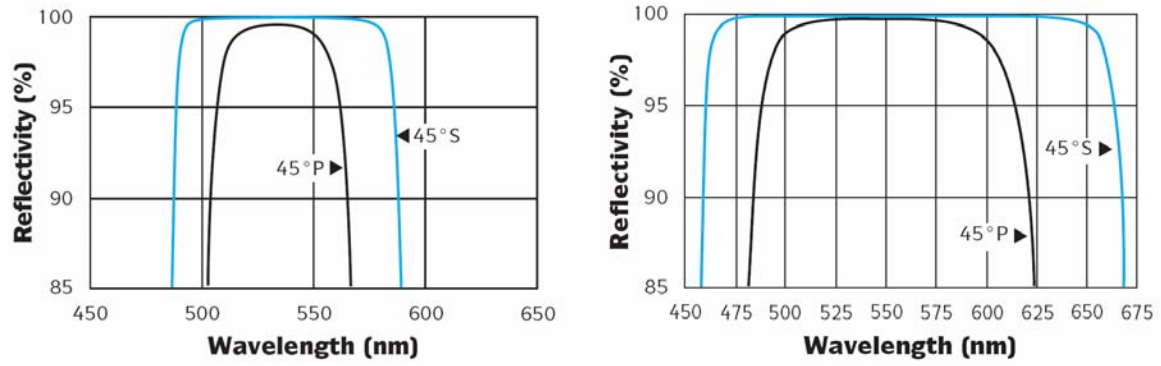

(A) YL2 ($275) (B) CV ($345)

Figure 3.10: (A) Reflectivity of a YAG laser mirror (YL2-2037-45-UNP) from CVI, and (B) reflectivity of a copper vapor laser mirror (CV-2037-45-UNP) from CVI.

3.4 Camera selection

The digital camera was selected based on the following three categories of criteria:

(1) Optical requirements for the digital camera

- Pixel size between 5 μm and 10 μm. For 50-MeV applications, a larger pixel size may be preferable for better efficiency
- Minimum number of pixels 1000 × 750

(2) Mechanical requirements for the digital camera

- Outside dimensions fit the envelope for tungsten shielding (not too big)

(3) Electrical requirements for the digital camera

- Camera Link or RS-644 interface
- Video frame rate at or greater than 10 frames per second at full resolution
- Remote electronic gain control desired in order to provide intensity control
- Data depth 10 to 12 bits
- Signal to noise ration > 50 dB

The last three criteria are important for imaging at low charge level.

At the time of writing, our top candidates are the Imperx models IPX-1M48, IPX-2M30, and IPX-2M30H. The main parameters of these Imperx IPX models are listed in Table 3.7. From the IPX-1M48 (1M pixel at 48 frames per second) up, all models meet our given criteria.

Table 3.7: Performance Parameters of Selected Imperx IPX Cameras

Model	**IPX-1M48**	**IPX-2M30**	**IPX-2M30H**
CCD sensor (Kodak)	KAI-1020	KAI-2020	KAI-2093
Maximum resolution	1004 × 1004	1600 × 1200	1920 × 1008
Pixel size	7.4 μm × 7.4 μm	7.4 μm × 7.4 μm	7.4 μm × 7.4 μm
CCD charge capacity	40 ke^-	40 ke^- / 20 ke^-	40 ke^- / 20 ke^-
Maximum output data depth	12 bit	12 bit	12 bit
Signal-to-noise ratio	60 dB	60 dB	60 dB
Maximum frame rate (dual tab)	48 fps	33 fps	33 fps
Analog gain range (remote control)	0 – 32 dB	6 – 38 dB	6 – 38 dB
Power consumption	3.6 W	4.8 W	4.8 W
Dimensions (mm)	67 × 67 × 41	67 × 67 × 47	67 × 67 × 47

3.5 Resolution estimate

Optical transition radiation has been used for imaging electron beam for decades [11]. It has been shown recently that resolutions under 5 μm can be achieved with OTR screens and appropriate optics [12-14]. We notice that uncertainties in beam size measurements come from many sources: diffraction limit, optical aberration, camera element size, screen/optics defect, calibration error, and photon statistics. In a conservative estimate (over-estimate), we can add these uncertainties (resolution) quadrature

$$\sigma_{res}^2 = \sigma_{diff}^2 + \sigma_{optics}^2 + \sigma_{camera}^2 + \sigma_{defect}^2 + \sigma_{stat}^2 , \tag{3.12}$$

where the meaning of the symbols are explained in Table 3.8.

Table 3.8: Budget for Spatial Resolution from Different Sources

Diffraction limited resolution for OTR screen, σ_{diff}	5 μm
Aberration of the imaging optics, σ_{optics}	9 μm
Resolution of camera sensor, σ_{camera}	3 μm
Uncertainty from manufacturing defect, σ_{defect}	3 μm
Uncertainty from finite statistics, σ_{stat}	4 μm
Total resolution, σ_{res}	12 μm

3.5.1 List of optical components and distances

Table 3.9 lists the camera's optical components. Table 3.10 shows the distances / locations of the components in the current design.

Table 3.9: List of Imaging Optics Components

Component	Vendor	Part number	Thickness	Comment
Viewport	MDC	VP-450QZ	3.2 mm	Fused silica
Lens L1	Newport	PAC089	14 mm	f_1 = 300 mm achromat
Lens L2	Newport	PAC089	14 mm	f_2 = 300 mm achromat

Table 3.10: Distances Between Imaging Optical Elements

Component	Distance (mm)	Comment
OTR screen	0.00	Light source
Reflecting mirror	150	First mirror 1/4" from the source center
Viewport (1st surface)	100	Viewport, 1/8" thick
Lens L1 (1st surface)	40	300 mm achromat lens, 7 mm thick
Lens L2 (1st surface)	50*	300 mm achromat lens, 7 mm thick
Camera	**290* from L2 last surface**	Camera CCD surface

* Important distance, +0.25"/-0.25" adjustable

3.5.2 Estimate diffraction-limited resolution

Applying Huygens principle on the angular distribution of the OTR light, Eq. (3.1), an approximate point spread function (PSF) can be derived [12]:

$$\left|E_x\right|^2 \sim \left(\frac{1-J_0\left(x/\Lambda_0\right)}{x/\Lambda_0}\right)^2, \left(\Lambda_0 = \lambda\!\!\!^{-}/\theta_0\right). \tag{3.13}$$

The PSF is a ring with a radius ~ $2.8\cdot\Lambda_0$ (Figure 3.11A). Integration of the intensity over *y*-coordinates resulted in a double-peaked profile of *x*-coordinates (Figure 3.11B).

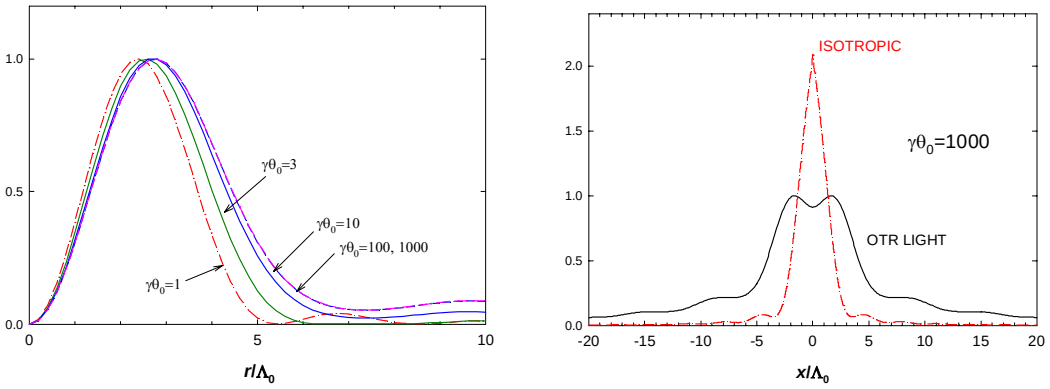

Figure 3.11: Diffraction-limited OTR intensity distributions: (A) point spread function in radial coordinates, (B) vertically integrated profile.

Fitting the profile to Gaussian functions [7,15] results in an estimate for diffraction-limited resolution for unpolarized OTR:

$$\sigma_{res} \approx \frac{4.2\cdot\lambda\!\!\!^{-}}{\theta_{1/2}}, \tag{3.14}$$

which is about 3.5 times the Gaussian radius of the PSF if the same optics are used to image an isotropic point source ($\sim 1.2 \cdot \lambda / \theta_{1/2}$). For wavelengths of 400 – 700 nm (OTR light) and aperture diameter of 50 mm, we have

$$\sigma_{res,diff} \approx \frac{4.2 \times 0.4 \times 300}{2\pi \times 25} = 3.2 \text{ [μm]}, (\lambda = 400 \text{ nm}), \quad (3.15)$$

and

$$\sigma_{res,diff} \approx \frac{4.2 \times 0.7 \times 300}{2\pi \times 25} = 5.6 \text{ [μm]}, (\lambda = 700 \text{ nm}). \quad (3.16)$$

Hence we can use an average value of 5 μm as the diffraction-limited resolution over the entire visible region.

Inserting a *y*-polarizer would further improve the resolution in the *x*-direction by about a factor of two [13,14]. However, we will not use this approach since it also reduces efficiency by a factor of two.

3.5.3 Estimate aberrations: ray tracing

Optical aberrations were estimated using a ray-tracing program ZEMAX [16]. A monochromatic ray tracing was performed first at 550 nm to estimate spherical aberration. Several polychromatic ray tracings were performed next by using the following weights in the wavelength table (Tables 3.11A through 3.11E).

Table 3.11A: Wavelengths and Weight for the Polychromatic Ray Tracing (490 nm – 565 nm)

Wavelength (nm)	490	500	510	520	530	540	550	560
Weight	1	1	1	1	1	1	1	1

Table 3.11B: Wavelengths and Weight for the Polychromatic Ray Tracing (515 nm – 585 nm)

Wavelength (nm)	520	530	540	550	560	570	580
Weight	1	1	1	1	1	1	1

Table 3.11C: Wavelengths and Weight for the Polychromatic Ray Tracing (470 nm – 645 nm)

Wavelength (nm)	475	500	525	550	580	610	640
Weight	1	1	1	1	1	1	1

Table 3.11D: Wavelengths and Weight for the Polychromatic Ray Tracing (500 nm – 700 nm)

Wavelength (nm)	500	550	600	650	700
Weight	1	2	2	2	1

Table 3.11E: Wavelengths and Weight for the Polychromatic Ray Tracing (400 nm – 700 nm)

Wavelength (nm)	425	475	525	575	625	675
Weight	1	1	1	1	1	1

Table 3.12 summarizes the ray-tracing results for a pair of Newport achromat lenses arranged back to back in 1:1 magnification (Table 3.9). We can see that the chromatic aberration has the dominant contribution, and a bandpass filter is desired if we want to match the geometric aberration to the diffraction limit. We want to emphasize that the OTR has an anisotropic distribution and the actual aberration is much less than Table 3.12 indicates. An improved

analysis will be presented in the next design report.

Table 3.12: RMS Size of the PSF from Geometrical Aberration at the Image (2 × PAC089)

Aperture size (mm)	RMS spot size (μm)					
	550 nm	490–565 nm	515–585 nm	475–645 nm	500–700 nm	400–700 nm
10	0.05	0.8	1.7	1.7	2.9	3.8
15	0.17	1.6	2.5	2.3	4.4	5.8
20	0.36	2.0	3.3	3.2	5.7	7.8
25	0.64	2.9	3.9	3.9	7.0	9.8
30	1.00	4.4	4.4	4.9	8.3	12.0
35	1.37	3.6	5.0	6.0	9.4	14.4
40	1.66	4.5	5.4	7.2	10.5	17.0
45	1.78	5.6	5.8	8.6	11.4	20.0
48	1.71	**6.3**	**6.0**	**9.5**	11.9	22.0
50	1.62	6.9	6.4	10.2	12.2	23.4

Comparing Table 3.12 with our resolution budget, we conclude that the resolution target can be reached with three bandpass filter configurations: (1) a YL2 mirror, (2) a 550 ± 35 nm interference filter, and (3) a CV mirror. We will use the last configuration as our baseline design since it also has the best photon efficiency.

4. Summary and Conclusion

We have completed the first-round design study for the LCLS undulator OTR imager. It will meet the physics requirements and technical specifications for the imager specified in relevant documents. The prototype design has two unique features: (1) it uses near-normal-incidence OTR screens to put the entire screen in focus at the same time, and (2) it uses a multilayer coated mirror to select imaging wavelength with high optical efficiency. With 12-μm rms resolution and electronic intensity control, the OTR imager will be able to take single-shot images of the LCLS electron bunch with only 0.2 nC charge.

This design was presented at SLAC on June 10, 2005, along with reviews of the Physics Requirements Document and Engineering Specification Document. Two issues came as valuable feedbacks for the presentation:

(1) SLAC is designing the OTR screen, and we may use it for beam test.

(2) Paul Emma pointed out a special operating mode where a 0.1-nC electron bunch will have 15-μm rms radius.

To support the low-emittance operation, we will need to improve the spatial resolution (to 8 μm or better) and charge sensitivity (0.1 nC or better) for at least one OTR station. We will need to (1) shorten the optical path and focal lengths of the imaging lenses, possibly by reducing radiation shielding requirements; (2) recalculate the aberrations with correct angular distribution; and (3) consider using the all mirror configuration shown in Figure 3.5B. We will address these issues in a future report for this project.

5. References

[1] J. Arthur et al., "LCLS Conceptual Design Report," SLAC-R-593, http://www-ssrl.slac.stanford.edu.

[2] B. Yang, "Physics Requirements for LCLS Undulator OTR Beam Profiler," LCLS Physics Requirement Document 1.4-004 (LCLS/ANL Document # L1450205-00034).

[3] J. Bailey, "Technical Specifications for LCLS Undulator OTR Beam Profiler," LCLS Engineering Specification Document 1.4-109 (LCLS/ANL Document # L1450205-00033).

[4] H. Nuhn, "LCLS Undulator Requirements," LCLS Specification 1.4-001.

[5] B. X. Yang et al., "Design and Performance of a Compact Imaging System for the APS Linac Bunch Compressor," PAC'01, Chicago, June 2001, p. 2335.

[6] A. W. Chao, ed., *Handbook of Accelerator Physics and Engineering*, World Scientific, Singapore, 1999, p. 190.

[7] B. X. Yang, "Optical System Design for High-energy Particle Beam Diagnostics," BIW'02, BNL, May 2002, AIP Conf. Proc. 648, p. 59.

[8] A. Murokh et al., "Limitations on Measuring a Transverse Profile of Ultra-Dense Electron Beams with Scintillators," PAC'01, Chicago, June 2001, p. 1333.

[9] W. J. Smith, *Modern Optical Engineering*, 2nd ed., Boston, MA, McGraw-Hill, 1990, p. 52.

[10] A. Specka et al., "High Resolution Beam Monitoring with Optical Transition Radiation at 3 MeV Electron Energy," PAC'01, Chicago, June 2001, p. 1333.

[11] D. Rule, Nucl. Nucl. Instrum. Methods B24/25 (1987) 901.

[12] V.A. Lebedev, Nucl. Instrum. Methods A372 (1996) 344.

[13] M. Castellano and V. A. Verzilov, Phys. Rev. ST Accel. Beams 1, 062801 (1998).

[14] M. Ross et al., "Very High Resolution Optical Transition Radiation Beam Profile Monitor," BIW02, BNL, May 2002, AIP Conf. Proc. 648, p. 237.

[15] B. X. Yang et al., "Design of a High-Resolution Optical Transition Radiation Imager for the Linac Coherent Light Source Undulator," PAC'05, Knoxville, May 2005, to be published.

[16] ZEMAX ray-tracing program (www.zemax.com).